Available online at www.sciencedirect.com
SCIENCE DIRECT®
Materials Chemistry and Physics 82 (2003) 750–757
MATERIALS CHEMISTRY AND PHYSICS
www.elsevier.com/locate/matchemphys

Lithium intercalation in graphites precipitated from pig iron melts

Y.H. Lee [a], K.C. Pan [a], Y.Y. Lin [b], T. Prem Kumar [b,1], G.T.K. Fey [b,*]

[a] *Institute of Materials Research and Engineering, National Taiwan University, 1 Roosevelt Road, Section 4, Taipei 106, Taiwan, ROC*

[b] *Department of Chemical and Materials Engineering, National Central University, Chung-Li 32054, Taiwan, ROC*

Received 18 March 2003; received in revised form 30 June 2003; accepted 4 July 2003

Abstract

The structural and electrochemical properties of graphitic materials precipitated from supersaturated solutions of carbon in pig iron melts were investigated. Doping of the graphite with boron was accomplished by adding ferroboron to the iron melt. X-ray diffraction patterns showed that all the products were highly crystalline graphites, and that doping with boron generally reduced the d_{002} values, which indicated that boron was incorporated in the hexagonal graphite matrix. Boron incorporation also led to a break in the local symmetry of the graphitic structure, as evidenced by the evolution of the D-band of the Raman spectra with an increase in the boron content. Scanning electron micrographs revealed the presence of nanocarbon structures on the surface of the graphites. The first-cycle capacity of the graphites was found to increase as the boron content was increased. However, the capacities of the boron-free and 60 ppm boron-doped materials abruptly increased in the second cycle, while the capacity of the 300 ppm boron-doped graphite remained fairly steady. All the graphites cycled well. The boron-free, 60 ppm boron-doped and the 300 ppm boron-doped graphites, sustained 198, 203 and 180 cycles, respectively, before reaching a charge retention level of 80%.

Keywords: Graphitic carbon; Carbonaceous anode; Boron-doped carbon; Catalytic graphitization; Lithium-ion batteries

1. Introduction

In the last two decades, numerous carbonaceous materials, both natural and synthetic, have been examined for their lithium intercalation properties for possible application as anodes in lithium-ion batteries. Several of these carbons have a disordered structure, often containing substantial amounts of hydrogen, and have demonstrated lithium insertion capacities much larger than the 372 mAh g^{-1} theoretically possible with perfectly graphitic structures. However, their applicability in practical cells is limited by large hysteresis in their charge–discharge profiles [1–3] (for hydrogen-containing carbons), and high irreversible capacities [1,4,5] even after several cycles [6,7]. On the other hand, graphitic carbons have only moderately high lithium storage capacities. However, their relatively flat potential profiles near the redox potential of the Li^+/Li couple, good reversibility for the lithium intercalation process, safety, non-toxicity and low cost make them attractive as lithium insertion anode materials. Thus, much effort has been expended in the synthesis and evaluation of various carbons with graphite-like characteristics.

Graphitic materials investigated have been either natural or synthetic ones, often graphitized at high temperatures. Although graphites have similar crystallographic structures, their electrochemical characteristics can be different [8–10], depending on their surface texture, surface functional groups, etc. The approaches adopted to improve the capacity of graphitic carbons include synthesis of newer varieties, surface treatment, and structural modification by doping with nitrogen, phosphorus or boron. A disadvantage of these approaches is their energy-intensive high-temperature processing, typically in the 2300–2800 °C range [11]. Production of graphitic carbons with good layer characteristics at temperatures below 2000 °C would be a welcome development in anode material research. In this work, we report the electrochemical properties of graphites obtained by precipitation from a supersaturated solution of carbon in a pig iron melt. The graphitization was effected at 1600 °C. The effect of boron as a dopant in the graphites on

* Corresponding author. Tel.: +886-3-422-7151extn.4206/425-7325; fax: +886-3-425-7325.
E-mail address: gfey@cc.ncu.edu.tw (G.T.K. Fey).
[1] On deputation from Central Electrochemical Research Institute, Karaikudi 630006, Tamil Nadu, India.

0254-0584/$ – see front matter © 2003 Elsevier B.V. All rights reserved.
doi:10.1016/S0254-0584(03)00374-2

the electrochemical lithium intercalation properties is also discussed.

2. Experimental

Graphitic carbon materials were prepared by catalytic graphitization of carbon in iron melts, as described elsewhere [12,13]. Briefly, the method involves the dissolution of an amorphous carbon in a melt of pig iron at 1600 °C in a reducing atmosphere to form a supersaturated solid solution of the carbon which subsequently precipitated as graphite when the melt is cooled. Doping with boron was done by adding ferroboron to the melt. The precipitated graphite was recovered by leaching the metallic constituents with 3 M HCl for 24 h, washing them with double distilled water, and drying. The products obtained are designated as PG-X, where PG stands for pig iron-derived graphite and X for the boron content in the melt in ppm. It should be noted that boron in the melt gets partitioned between the iron and carbon in the melt, so that only a fraction of the boron from the ferroboron will be incorporated in the graphite.

X-ray diffractograms of the graphites were recorded on a Philips PW-1710 X-ray diffractometer fitted with a nickel-filtered Cu Kα radiation source between scattering angles of 5° and 80° in steps of 0.05°. A Perkin-Elmer CHN-2000 elemental analyzer was used for the elemental composition of the products. The typical sample weight for elemental analysis was 3 mg. However, residual iron content in the graphitic product was determined by an ICP-MS model PE-Sciex Elan 6100DRC. The surface morphology of the graphites was examined by scanning electron microscopy (Hitachi S-4700I). Laser Raman spectroscopic measurements were performed in the 1000–2000 cm^{-1} region with a laser radiation wavelength of 632.8 nm (Renishaw G-17868 Raman spectrophotometer). The Raman results were fitted with Renishaw software.

The lithium intercalation–deintercalation properties of the graphite materials were studied in 2032-type coin cells with a lithium metal foil as the anode and a 1 M solution of $LiPF_6$ in a 1:1 (v/v) mixture of EC:DEC as the electrolyte. Graphite electrodes for the coin cells were fabricated as follows. The graphite powder was made into a slurry with 8% PVdF binder and 2% conducting carbon black additive in NMP. The slurry was coated on a copper foil using the doctor blade method. The coated foil was allowed to dry at 120 °C in an oven for 90 min, and roller-pressed to improve contact between the coated material and the current collector. Circular discs were punched out from the coated foil. Cell assembly was done in an argon-filled glove box (VAC Model MO40-1), where the moisture and oxygen levels were maintained below 2 ppm. Galvanostatic charging and discharging of the cells were done at a 0.1 C rate between 3.0 and 0.05 V in a multi-channel battery tester (Maccor Series-4000). Differential capacity plots were obtained from charge–discharge profiles.

3. Results and discussion

3.1. Elemental analysis

The compositions of the graphites are furnished in Table 1. It can be seen that the amount of iron retained in the samples after the 24 h acid-leaching was in ppm levels. The H/C ratios were about 0.1. The nitrogen in the samples is thought to originate from the inert atmosphere over the melt. The unaccounted part of the composition is attributed to unleached constituents, such as silicon, present in the pig iron.

3.2. X-ray diffraction

The crystallization of amorphous carbon into graphite when a supersaturated melt of carbon in iron is cooled has been well documented [14–17]. The graphitization process is believed to be due to either the G effect [16,17], a process by which carbon dissolves in the iron and precipitates out as graphite, or to the formation and decomposition of carbide intermediates [15,17]. According to Oberlin and Rouchy [15], melting a non-graphitic carbon with iron results in the formation of a composite of graphite and a graphitizable phase. It is believed that an unstable phase of iron carbide is formed, which subsequently decomposes to yield iron globules surrounded by shell of graphitizable carbon [15].

The X-ray diffraction patterns of the graphites (Fig. 1) show sharp peaks, suggesting a high degree of crystallinity. All the patterns show a strong peak at a 2θ value of around 26°, corresponding to the (0 0 2) reflection. The reflections corresponding to the other $h\,k\,l$ indices are comparatively weak, and are shown in the insets. Diffraction peaks were also observed around 2θ values of 13° and 17°, which are attributed to nanocarbon structures. In an earlier communication on graphite synthesized from cast iron melts [12], we showed by a Rietveld analysis of the X-ray diffraction data that the graphites contained as much as 4% by weight fullerene molecules.

The interlayer spacing (d_{002}) did not change between the PG-0 and PG-60 graphites (Table 2), probably because the doping level was too low. However, when the boron concentration was raised to 300 ppm, the d_{002} value dropped, suggesting that boron was incorporated in the hexagonal graphitic layers [18]. Substituting boron in carbons up to

Table 1
Elemental analytical data on the graphitic materials

Graphite type	Elemental analysis				
	Fe[a]	C (%)	H (%)	N (%)	H/C ratio
PG-0	9.63	92.40	0.78	0.56	0.10
PG-60	28.70	94.13	1.03	0.56	0.13
PG-300	14.90	94.42	0.60	1.08	0.08

[a] Analyzed by ICP-MS; concentration in ppm.

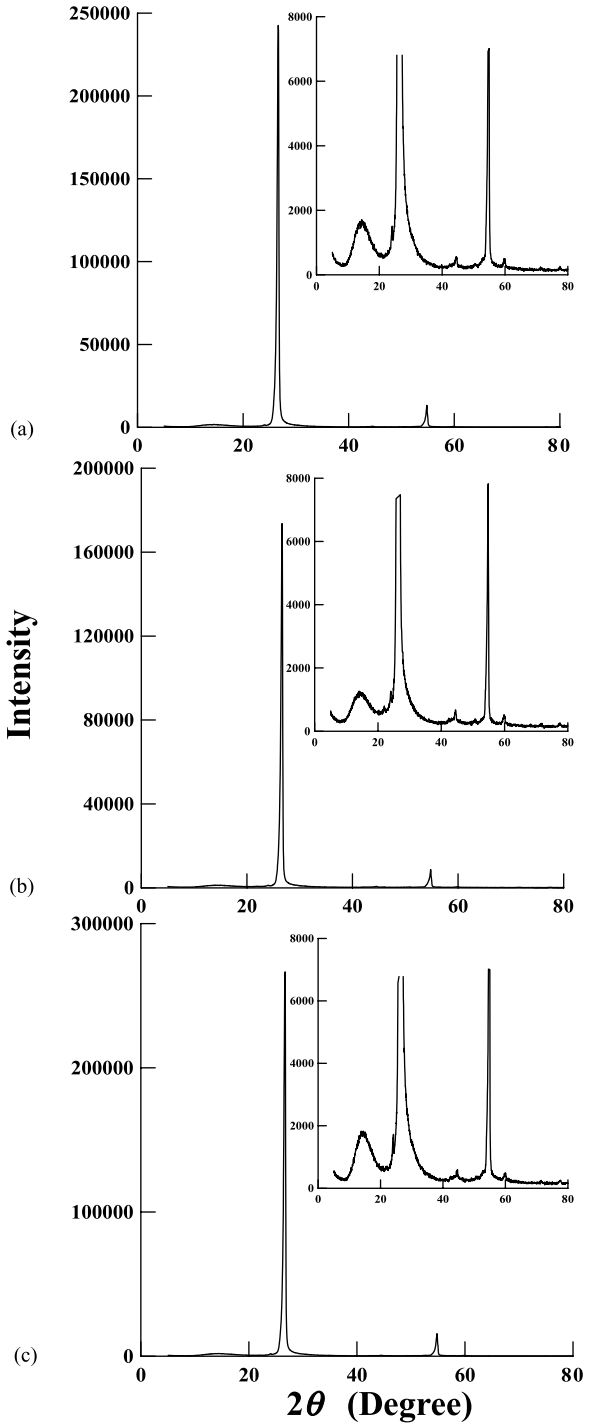

Fig. 1. X-ray diffractograms of graphitic materials with different boron concentrations: (a) PG-0; (b) PG-60; (c) PG-300. The peaks of the minor indices are given in the insets.

Table 2
Interlayer spacing (d_{002}, Å) as a function of the boron content

Boron content (ppm)	Carbon layer spacing, $d_{(002)}$ (Å)
0	3.342
60	3.342
300	3.336

2.35 at.% has been shown to decrease the d_{002} spacing [19,20]. Endo et al. [21] showed that boron doping of mesophase pitch-based carbon fibers led to a more developed *c*-axis crystallite structure. The effect of boron substitution on the d_{002} value is supposed to be related to the depleted π-electrons between the graphene layers, which lead to a contraction in the interlayer distance. The lower valency of boron in the structure is also believed to reduce the π-electron density within the graphene layers [22,23].

3.3. Scanning electron microscopy

According to Wang et al. [24], the structural and morphological characteristics of graphites produced by catalytic graphitization depend on the nature of the precursors and the thermal history. From the SEM images shown in Fig. 2, it can be seen that all the products had a flaky appearance. The large flakes are as big as 5–8 μm across. A large proportion of small flaky crystallites were also present. Flakiness is a characteristic of graphites precipitated from carbon-rich iron melts [25,26]. If carbon atoms are assumed to be present as interstitials in a matrix of liquid iron [27], molecular assemblies of carbon may be expected to form by strong bonding in the *a*-direction according to the 'chicken-wire' model [28]. The resulting hexagonal monolayers then bond in the *c*-direction to give an intermediate three-dimensional lattice of micro-column and wrinkled graphites, which eventually transform into stiff flakes of graphite [29,30].

Fig. 3 shows the high-resolution SEM images of PG-0, PG-60 and PG-300. In addition to the extensive micro-flakiness, some filamentous structures were observed in the SEM images of the graphites. The high-charge density areas, seen as bright areas, indicate the presence of these nanostructures. Rodriguez [31] reported that such structures could be formed from hydrocarbons on metal substrates, although some of the products required as much as 3000 °C for their graphitization. The formation mechanism of filamentous or tubular structures by rolling or wrapping planar graphene layers is unclear, but it appears that they could be generated by molecular addition in the *c*-direction. However, their growth potential is small [27], which explains the limited formation of nanoscale structures.

3.4. Raman spectroscopy

Raman spectroscopy is a useful tool for the study of carbons because Raman spectral response is sensitive to the microscopic structure of the carbon. Raman spectra of the graphites are shown in Fig. 4. Two bands can be seen in all the spectra: one, the D-band around 1355 cm^{-1}, and the other, the G-band around 1580 cm^{-1}. The G-band is an inherent Raman-active band for the ideal graphite structure, corresponding to the E_{2g} vibration mode [32], and ascribed to the C–C stretching in the longitudinal symmetry axis of the graphite plane [33,34]. The D-band, usually identified as the A_{1g} mode, is forbidden for the two-dimensional lattice

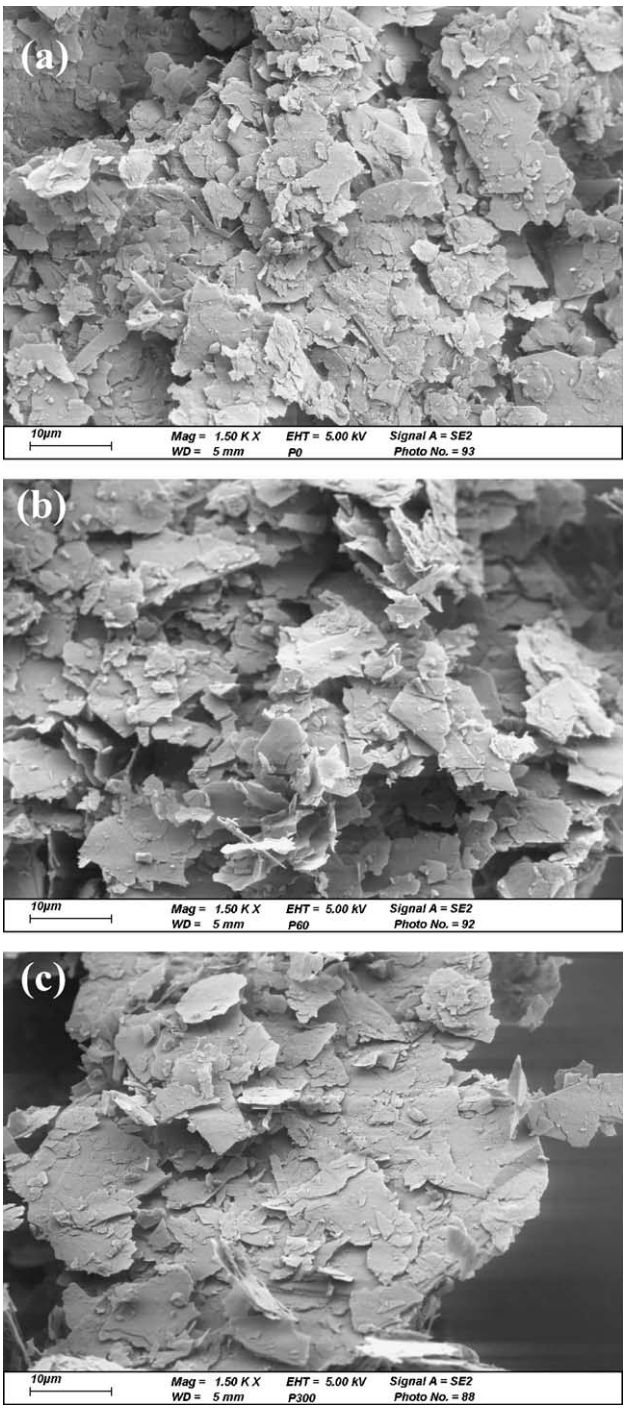

Fig. 2. Scanning electron micrographs of (a) PG-0, (b) PG-60 and (c) PG-300 graphites.

of graphite according to selection rules, and is a subject of controversy [35]. However, for graphite crystallites of finite sizes, the A_{1g} mode will become Raman-active [36]. This band is assigned to defects on the boundary of the carbon layers. For comparison, the Raman spectrum of the amorphous carbon employed in this study is also shown in Fig. 4. It can be seen that the broad D-band in the amorphous carbon became narrower and lower in intensity after graphiti-

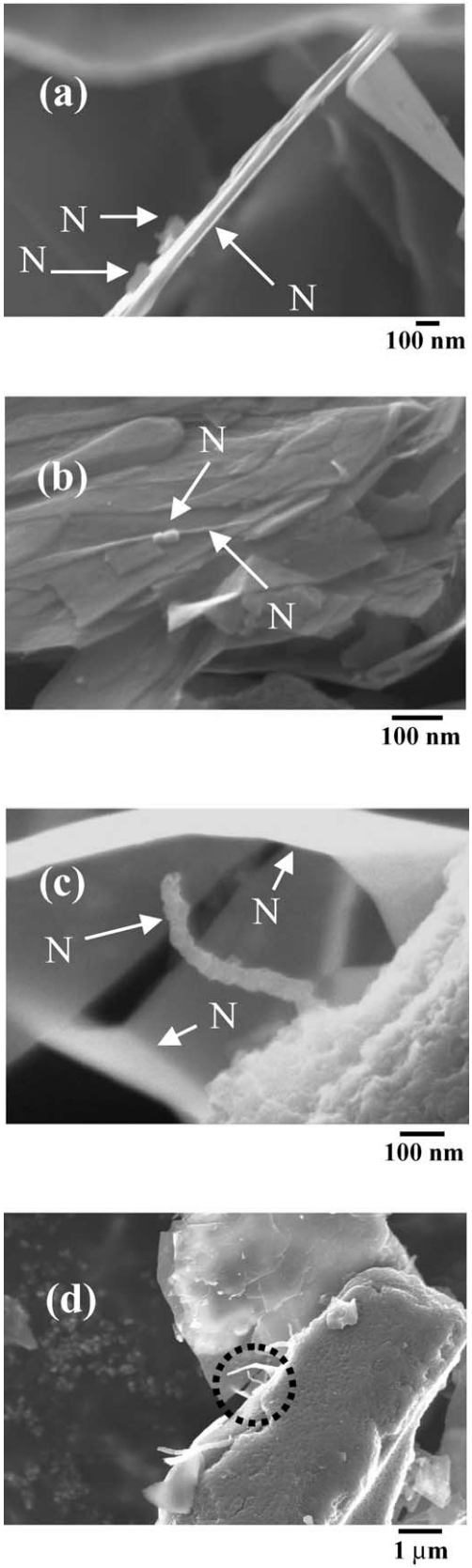

Fig. 3. High-resolution scanning electron micrographs of (a) PG-0, (b) PG-60 and (c) PG-300. The area from which (c) was zoomed is indicated in (d). The nanostructures are indicated by the letter N.

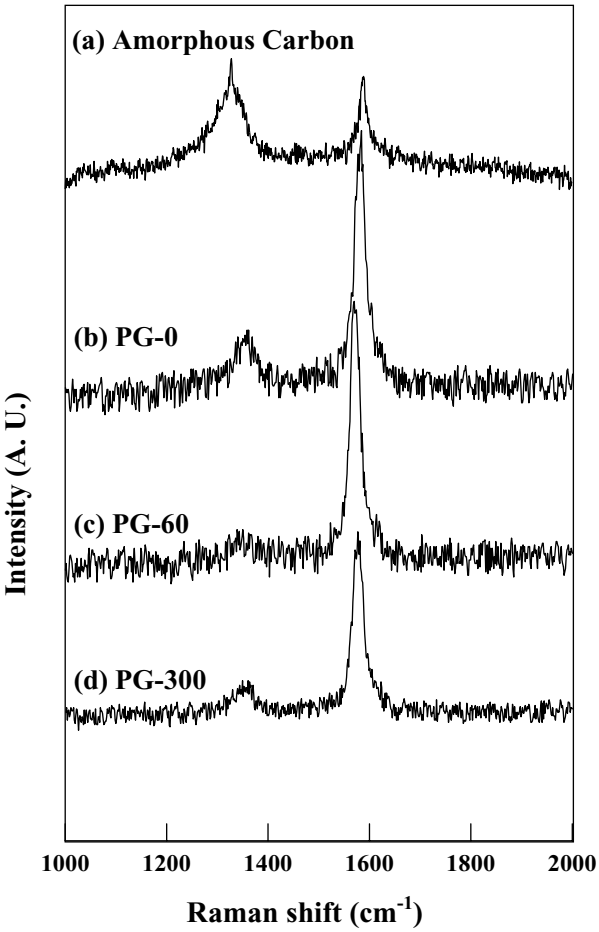

Fig. 4. Raman spectra of graphitic materials with different boron concentrations.

zation. The G-band also became sharper, indicating a high degree of graphitization in the products.

An additional feature in the spectra of the boron-doped samples is the 1620 cm^{-1} band, which corresponds to the maximum phonon density of states. Boron in the graphite lattice should be present as sp^2 hybridized atoms. Both the 1355 and the 1620 cm^{-1} bands are associated with local structural distortions, which must increase their intensity as more boron is incorporated into the graphite structure. Since the 1355 cm^{-1} band is ascribed to scattering from the zone-boundary phonons, which becomes Raman-active because of a loss of translational symmetry [37,38], increased boron doping should lead to symmetry breaking. This is evident from Fig. 4, which shows the evolution of these bands as the boron content was increased to 60 and 300 ppm.

Table 3
Characteristic Raman shifts and the integrated intensity ratios of the D- and G-bands for the various graphitic materials

Graphite type	Characteristic peak (cm^{-1})		I_D/I_G
PG-0	D	1362	0.31
	G	1584	
PG-60	D	1350	0.20
	G	1570	
PG-300	D	1360	0.24
	G	1577	

Table 3 shows the positions of the characteristic Raman bands and the integrated intensity ratios (I_D/I_G) of the graphite samples. The integrated intensity ratio is a measure of the orientation of the graphitic planes and the degree of graphitization [21]. I_D/I_G values for the boron-containing graphites are lower than that for the boron-free graphite, suggesting that the incorporation of boron led to a higher degree of graphitization. Boron substitution has been known to catalyze the graphitization process [39–43]. The noise in the spectra makes it difficult to draw more conclusions from the data.

3.5. Electrochemical studies

The graphites synthesized by the catalytic graphitization process were subjected to galvanostatic charge–discharge studies. Results for the first 10 cycles are given in Table 4. It can be seen that the first-cycle deintercalation capacities increased from 300 and 303 mAh g^{-1} for PG-0 and PG-60, respectively, to 365 mAh g^{-1} for PG-300. The lithium deintercalation capacities in the second cycle for PG-0 and PG-60 graphites jumped to 394 and 379 mAh g^{-1}, respectively. The higher capacity of the PG-300 graphite is in agreement with the increased capacities reported with several boron-doped carbons [44–48]. However, the capacity of PG-300 remained fairly steady as the cycling proceeded, while those of PG-0 and PG-60 registered an abrupt jump in capacity from the second cycle. Because pig iron is an impure form of iron

Table 4
Charge–discharge data for the different graphites for the first 10 cycles[a]

C.N.	PG-0				PG-60				PG-300			
	I.C.	D.C.	Ir.C.	C.E.	I.C.	D.C.	Ir.C.	C.E.	I.C.	D.C.	Ir.C.	C.E.
1	405	300	105	74	425	303	122	71	462	365	97	79
2	411	394	17	96	395	379	16	96	376	364	12	97
5	399	391	8	98	382	377	5	99	371	363	8	98
10	395	392	3	99	377	374	3	99	363	360	3	99

[a] I.C.: intercalation capacity (mAh g^{-1}); D.C.: deintercalation capacity (mAh g^{-1}); Ir.C.: irreversible capacity (mAh g^{-1}); C.E.: cycle efficiency (%); C.N.: cycle number.

obtained directly from the blast furnace, phases formed with such impurities as silicon may perhaps influence the lithium intercalation behavior of the graphitic products obtained with this iron. It can be seen from Table 4 that the first-cycle irreversible capacities of the graphites were 105, 122 and 97 mAh g^{-1}, which are in the 21–29% bracket. This value is considerably lower than commonly reported irreversible capacities. For example, Chang et al. [49] reported irreversible capacities of 25–38% for mesocarbon microbeads graphitized at 2400 °C.

3.5.1. Differential capacity plots

The intercalation of lithium into graphite occurs by a staging mechanism [50,51], which can be discerned from differential capacity plots. The differential capacity vs. voltage plots for the PG-0 and PG-300 graphites are shown in Fig. 5. The differential capacity plots were derived from the second cycle data of the galvanostatic charge–discharge experiments. As can be seen from Fig. 5(a), which shows the differential capacity plot of PG-0, there are three well-defined peak potentials during lithium intercalation (charging of graphite) at 0.23, 0.15 and 0.11 V. During the lithium deintercalation process, the peaks were observed at 0.06, 0.12 and 0.20 V. This shows that all the electrochemical events contributing to capacity occurred below 0.25 V. Above 0.25 V, there was no contribution to capacity. Similarly, as can be seen from Fig. 5(b), all the processes corresponding to the intercalation and deintercalation of lithium occur at potentials below 0.25 V vs. Li^+/Li for PG-300 too. Based on the potentials at which the peaks appear, the following stages can be ascribed [50,51]. The cathodic region up to around 0.20 V: dilute phase I to the fourth stage; the region between 0.20 and 0.09 V: fourth to the third stage, followed by the third to the second stage; and finally the region at more negative potentials: second to the first stage. In a similar study of boron-doped mesophase pitch carbon fiber, cyclic voltammetry showed peaks in the positive scan at 0.2, 0.1 and 0.05 V, whereas the peaks in the negative scan were observed at 0.12, 0.15 and 0.22 V [21].

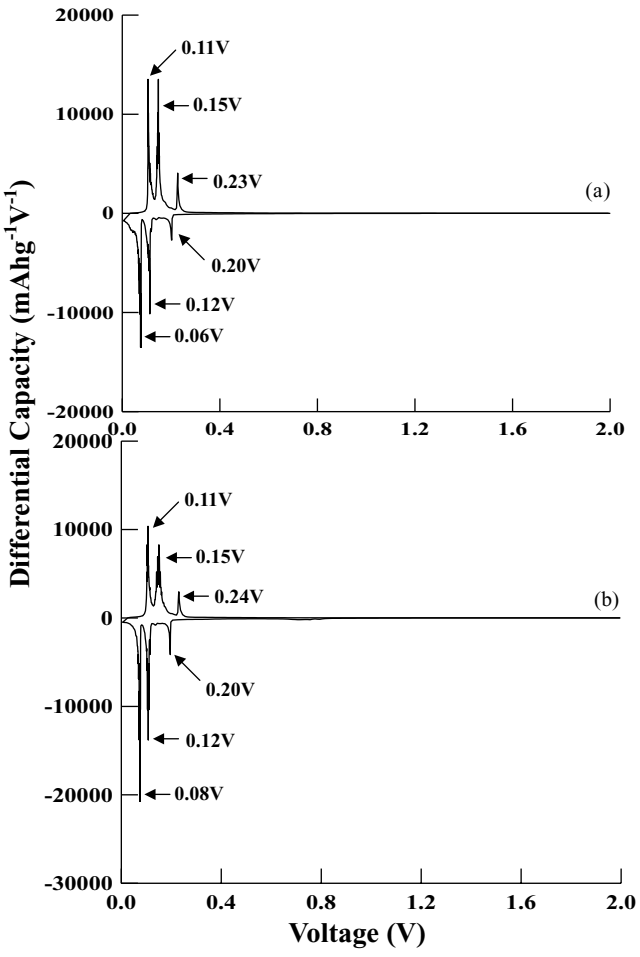

Fig. 5. Differential capacity vs. voltage plots for (a) PG-0 and (b) PG-300 graphites.

3.5.2. Cycling performance

We have already noted that an increase in boron content to 300 ppm significantly increased the first-cycle capacity of the graphite (Table 4). It can be seen from Fig. 6 that as cycling proceeded, the capacity of the boron-free and 60 ppm boron-doped graphites generally increased, and even remained steady at values above 372 mAh g^{-1}. A curious aspect of the cycling behavior of these graphites is a general rise in their capacity towards the end of their cycle-lives. Although we are unable to explain this pattern, it must be pointed out that the rise in capacity can serve as an end-of-life indication for cells that incorporate such anode materials. The increase is very pronounced in the case of PG-0, which delivered the maximum capacity of 454 mAh g^{-1}. Moreover, PG-0 and PG-60 gave consistently

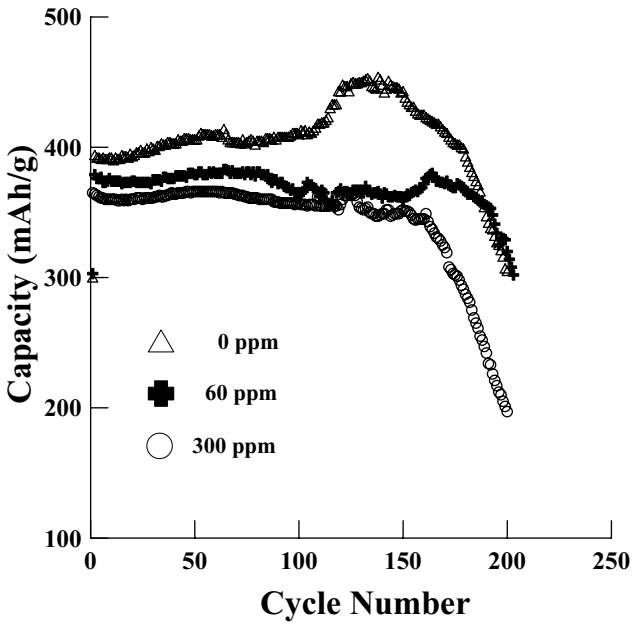

Fig. 6. Cycling behavior of PG-0, PG-60 and PG-300 graphites.

higher capacities than the 372 mAh g^{-1} theoretically obtainable from perfectly graphitic structures. Fig. 6 shows that for an 80% cut-off value for charge retention, based on the second-cycle capacity for PG-0 and PG-60 and the first-cycle capacity for PG-300, the number of cycles sustained were 198, 203 and 180, respectively, for the PG-0, PG-60 and PG-300 samples. It can be seen from Fig. 6 that although all the graphites consistently delivered high capacities over extended cycles, their capacities fell precipitously beyond the 80% capacity retention cut-off. Thus, the useful life of the graphites is restricted to the first 20% of their capacity. At greater depths of capacity retention, a rapid failure mechanism seems to set in. The fact that the capacity fade is not gradual suggests that the failure mode is not only suddenly triggered, but its action is rapid. Further experimentation is required to decipher this aspect of the cycling profiles.

The unusually high capacity of PG-0 deserves special attention. The X-ray diffraction studies showed no evidence of any amorphous phase. Therefore, any contribution from turbostratically disordered structures presenting additional lithium accommodation sites is discounted. Hydrogen content of the carbons is another factor contributing to capacities well above the theoretical value. The H/C ratio of this graphite was 0.10 (Table 1), which is not low for a carbon derived at temperatures as high as 1600 °C. However, this value is not large enough either to account for the 'excess' lithium capacity. The hydrogen is believed to 'saturate' the dangling bonds on the edge carbons of graphene fragments [52]. Papanek et al. [52] have shown by ab initio calculations that the energy required for lithium intercalation or for lithium to bind to these hydrogen-saturated sites is not very different. Thus, lithium intercalation and lithium binding to hydrogen-saturated carbons must occur at similar potentials, contributing to the excess lithium capacity. Another possible explanation for the increased lithium intercalation capacity is the presence of nanotubular structures, albeit in small amounts, on the surface of the catalytically graphitized materials [12]. Carbon nanotubes have been shown to yield lithium insertion capacities of as much as 1400 mAh g^{-1} [53–56]. We have seen from our SEM studies that the graphites have filamentous nanostructures on them. Thus, we believe that the 'excess' capacity in these graphites arises from these nanostructures, which, owing to their high specific charges, can contribute significantly to the capacity even though their concentrations are small. Further work is required to quantify the contribution of these nanotubular carbon structures to the capacity improvement of the graphites.

4. Conclusions

Electrochemical lithium intercalation properties of crystalline graphitic materials, prepared by the catalytic graphitization method in melts of pig iron were studied. The formation of highly crystalline graphites was realized at temperatures as low as 1600 °C. The X-ray diffractograms showed that the d_{002} values of PG-0 and PG-60 samples were the same but were lower for the PG-300 graphite, which shows that boron was incorporated in the hexagonal graphite matrix. Boron incorporation also led to a breaking of the local symmetry of the graphitic structure, as evidenced by the evolution of the D-band of the Raman spectra with an increase in the boron content. Although the boron-containing graphites showed higher first-cycle capacities, the presence of the dopant seemed to be slightly pejorative to the long-cycling performance of the graphites. All the graphites sustained nearly 200 charge–discharge cycles and had first-cycle irreversible capacities of 21–28%. The consistently high capacities above the 372 mAh g^{-1} mark obtained with these graphites are ascribed to nanocarbon structures that were formed during the catalytic graphitization process. In general, the graphites showed a hump in their capacity vs. cycle number curves, which could serve as an end-of-life indicator for cells that use them as anode materials.

Acknowledgements

This work was carried out under contract no. NSC-90-2214-E-008-051 of the National Science Council of the Republic of China. TPK thanks the NSC for the award of a post-doctoral fellowship.

References

[1] T. Zheng, J.S. Xue, J.R. Dahn, Chem. Mater. 8 (1996) 389.
[2] H. Fujimoto, A. Mabuchi, K. Tokumitsu, T. Kasuh, J. Power Sources 54 (1995) 440.
[3] S. Yata, Y. Hato, H. Kinoshita, N. Ando, A. Anekawa, T. Hashimoto, M. Yamaguchi, K. Tanaka, T. Yamabe, Synth. Met. 73 (1995) 273.
[4] Y. Mori, T. Iriyama, T. Hashimoto, S. Yamazaki, F. Kawakami, H. Shiroki, T. Yamabe, J. Power Sources 56 (1995) 205.
[5] J.S. Xue, J.R. Dahn, J. Electrochem. Soc. 142 (1995) 3668.
[6] M. Alamgir, Q. Zuo, K.M. Abraham, J. Electrochem. Soc. 141 (1994) L143.
[7] T. Iijima, K. Suzuki, Y. Matsuda, Synth. Met. 73 (1995) 9.
[8] S. Flandrois, A. Fevrier-Bouvier, K. Guerin, B. Simon, P. Biensan, Mol. Cryst. Liq. Cryst. 310 (1998) 398.
[9] R. Fong, U. von Sacken, J.R. Dahn, J. Electrochem. Soc. 137 (1990) 2009.
[10] P. Schoderbook, H.P. Boehm, Mater. Sci. Forum 91–93 (1992) 683.
[11] N. Tamaki, A. Satoh, M. Hara, T. Ohsaki, J. Electrochem. Soc. 142 (1995) 2564.
[12] Y.H. Lee, Y.C. Chang, K.C. Pan, S.T. Chang, Mater. Chem. Phys. 72 (2001) 232.
[13] Y.H. Lee, K.C. Pan, Y.Y. Lin, V. Subramanian, T. Prem Kumar, G.T.K. Fey, Mater. Lett. 57 (2003) 1113.
[14] S.B. Austerman, S.M. Myron, J.W. Wagner, Carbon 5 (1967) 549.
[15] A. Oberlin, J.P. Rouchy, Carbon 9 (1971) 39.
[16] W. Weisweiler, N. Subramanian, B. Terwiesch, Carbon 9 (1971) 755.
[17] A. Oya, S. Otani, Carbon 19 (1981) 391.
[18] T. Hagio, M. Nakamizo, K. Kobayashi, Carbon 27 (1989) 259.
[19] C.E. Lowell, J. Am. Ceram. Soc. 50 (1967) 142.
[20] K. Miyazaki, H. Yoshida, K. Kabayashi, Tanso 128 (1987) 2.
[21] M. Endo, C. Kim, T. Karaki, Y. Nishimura, M.J. Mathews, S.D.M. Brown, M.S. Dresselhaus, Carbon 37 (1999) 561.

[22] P.S. Grosewald, P.L. Walker, Tanso 61 (1970) 52.
[23] J.W. McClure, Phys. Rev. 119 (1960) 606.
[24] W. Wang, K.M. Thomas, R.M. Poultney, R.R. Willmers, Carbon 33 (1995) 1525.
[25] S. Liu, C.R. Loper, Carbon 29 (1991) 547.
[26] S. Liu, C.R. Loper, Carbon 29 (1991) 1119.
[27] D.D. Double, A. Hellawell, Acta Metall. Mater. 43 (1995) 2435.
[28] D. Ugarte, Chem. Phys. Lett. 207 (1993) 473.
[29] Z. Zheng, J. Chin. Electron Microsc. 9 (1990) 237.
[30] Z. Zheng, Acta Mineral. Sin. 11 (1991) 214.
[31] N.M. Rodriguez, J. Mater. Res. 8 (1993) 3233.
[32] F. Tunistra, J.L. Koenig, J. Phys. Chem. 53 (1970) 1126.
[33] C. Mapelli, C. Castiglioni, G. Zerbi, K. Mullen, Phys. Rev. B 60 (1999) 12710.
[34] A.C. Ferrari, J. Robertson, Phys. Rev. B 61 (2000) 14095.
[35] R. Escribano, J.J. Sloan, N. Siddique, N. Sze, T. Dudev, Vib. Spectrosc. 26 (2001) 179.
[36] Z. Zheng, X. Chen, Sci. Chin. B 38 (1995) 97.
[37] T. Hagio, M. Nakamizo, K. Kobayashi, Carbon 27 (1989) 259.
[38] T.C. Chieu, M.S. Dresselhaus, M. Endo, Phys. Rev. B 26 (1982) 5867.
[39] R.B. Trask, Fuel 47 (1968) 397.
[40] H.N. Murty, D.L. Biederman, E.A. Heintz, Fuel 56 (1977) 305.
[41] A. Oya, R. Yamashita, S. Otani, Fuel 58 (1979) 495.
[42] T. Sogabe, K. Nakajima, M. Inagaki, J. Mater. Sci. 31 (1996) 6469.
[43] M. Inagaki, H. Konno, T. Tsumura, T. Nakahashi, T. Sogabe, H. Sato, Trans. Mater. Res. Soc. Jpn. 23 (1998) 5.
[44] M. Morita, T. Hanada, H. Tsutsumi, Y. Matsuda, M. Kawaguchi, J. Electrochem. Soc. 139 (1992) 1227.
[45] J.R. Dahn, J.N. Reimers, A.K. Sleigh, T. Tiedje, Phys. Rev. B 45 (1992) 3773.
[46] B.M. Way, J.R. Dahn, T. Tiedje, K. Myrtle, M. Kasrai, Phys. Rev. B 46 (1992) 1697.
[47] B.M. Way, J.R. Dahn, J. Electrochem. Soc. 141 (1994) 907.
[48] W. Cermignani, T.E. Paulson, C. Onneby, C.G. Pantano, Carbon 33 (1995) 367.
[49] Y.C. Chang, H.J. Sohn, C.H. Ku, Y.G. Wang, Y. Korai, I. Mochida, Carbon 37 (1999) 1285.
[50] J.R. Dahn, Phys. Rev. B 44 (1991) 9170.
[51] T. Ohzuku, Y. Iwakoshi, K. Sawai, J. Electrochem. Soc. 140 (1993) 2490.
[52] P. Papanek, M. Radosavlijevic, J. Fischer, Chem. Mater. 8 (1996) 1519.
[53] J.C. Withers, R.O. Loutfy, J.P. Lowe, Fullerene Sci. Technol. 5 (1997) 1.
[54] V.A. Nalimova, D.F. Skovsky, G.N. Bondarenko, H.A. Gaucher, G. Bonamy, F. Beguin, Synth. Met. 88 (1997) 89.
[55] G.T. Wu, C.S. Wang, X.B. Zhang, H.S. Yang, Z.F. Qi, P.M. He, W.Z. Li, J. Electrochem. Soc. 146 (1999) 1698.
[56] T. Prem Kumar, A.M. Stephan, P. Thayananth, V. Subramanian, S. Gopukumar, N.G. Renganathan, M. Raghavan, N. Muniyandi, J. Power Sources 97–98 (2001) 118.